

EUHFORIA modelling of the Sun-Earth chain of the magnetic cloud of 28 June 2013

G. Prete^{1,*}, A. Niemela^{3,4,*}, B. Schmieder^{3,5}, N. Al-Haddad⁶, B. Zhuang⁶, F. Lepreti^{1,2}, V. Carbone^{1,2}, and S. Poedts^{3,7}

- Department of Physics, University of Calabria, Ponte P. Bucci 31C, 87036 Rende, CS, Italy e-mail: giuseppe.prete@unical.it
- National Institute for Astrophysics, Scientific Directorate, Viale del Parco Mellini 84, 00136 Roma, Italy
- ³ Centre for Mathematical Plasma Astrophysics, Dept. of Mathematics, KU Leuven, Celestijnenlaan 200B, 3001 Leuven, Belgium
- ⁴ Solar-Terrestrial Centre of Excellence-SIDC, Royal Observatory of Belgium, 1180 Brussels, Belgium
- ⁵ LESIA, Observatoire de Paris, PSL Research University, CNRS Sorbonne Université, Univ. Paris 06, Univ. Paris Diderot, Sorbonne Paris Cité, 5 place Jules Janssen, 92195 Meudon, France
- ⁶ Institute for the Study of Earth, Oceans, and Space, University of New Hampshire, Durham, NH, USA
- ⁷ Institute of Physics, University of Maria Curie-Skłodowska, Pl. M. Curie-Skłodowska 5, 20-031 Lublin, Poland

Received 15 May 2023 / Accepted 21 November 2023

ABSTRACT

Context. Predicting geomagnetic events starts with an understanding of the Sun-Earth chain phenomena in which (interplanetary) coronal mass ejections (CMEs) play an important role in bringing about intense geomagnetic storms. It is not always straightforward to determine the solar source of an interplanetary coronal mass ejection (ICME) detected at 1 au.

Aims. The aim of this study is to test by a magnetohydrodynamic (MHD) simulation the chain of a series of CME events detected from L1 back to the Sun in order to determine the relationship between remote and in situ CMEs.

Methods. We analysed both remote-sensing observations and in situ measurements of a well-defined magnetic cloud (MC) detected at L1 occurring on 28 June 2013. The MHD modelling is provided by the 3D MHD European Heliospheric FORecasting Information Asset (EUHFORIA) simulation model.

Results. After computing the background solar wind, we tested the trajectories of six CMEs occurring in a time window of five days before a well-defined MC at L1 that may act as the candidate of the MC. We modelled each CME using the cone model. The test involving all the CMEs indicated that the main driver of the well-defined, long-duration MC was a slow CME. For the corresponding MC, we retrieved the arrival time and the observed proton density.

Conclusions. EUHFORIA confirms the results obtained in the George Mason data catalogue concerning this chain of events. However, their proposed solar source of the CME is disputable. The slow CME at the origin of the MC could have its solar source in a small, emerging region at the border of a filament channel at latitude and longitude equal to +14 degrees.

Key words. magnetohydrodynamics (MHD) - shock waves - methods: numerical - interplanetary medium

1. Introduction

Coronal mass ejections (CMEs) are extreme energetic large-scale eruptions of plasma and magnetic field from the solar atmosphere, and they are considered to be one of the main drivers of strong space weather disturbances (Webb & Howard 2012; Kilpua et al. 2017b). The frequency of their occurrence depends on the phase of the solar activity cycle and can be as high as ten per day during solar maximum. CMEs are frequently associated with flux rope (FR) eruptions, either in active regions or in filament channels (Gopalswamy et al. 2003; Li et al. 2012; Schmieder et al. 2013). These FR structures have a closed magnetic field configuration in which 'free' (non-potential) magnetic energy is stored. When these structures become unstable, they erupt, releasing plasma and magnetic field into the heliosphere in the form of CMEs.

Using in situ measurements, it is possible to analyse the heliospheric counterpart of CMEs called interplanetary coronal mass ejections (ICMEs; Gosling et al. 1991; Song et al.

2020; Kilpua et al. 2017a; Davies et al. 2021; Zhang et al. 2021). In the last decades, the investigation of ICMEs has increased and improved due to the availability of multi-spacecraft measurements, which combine measurements from the Solar-Terrestrial Relations Observatory (STEREO; Kaiser et al. 2008), the Advance Composition Explorer (ACE), and Wind (Van der Harten & Clark 1995) while also using measurements from planetary missions (Kilpua et al. 2009, 2013; Winslow et al. 2016; Lugaz et al. 2020), remote heliospheric observations, and numerical simulations (Sow Mondal et al. 2021; Taktakishvili et al. 2010). This has allowed the scientific community to better understand the formation and propagation of ICMEs and their interaction with other transients.

The classical signature of the passage of a fast ICME over a spacecraft in the inner heliosphere is identified by a sharp enhancement of the total magnetic field strength and the radial velocity, which corresponds to the passage of the shock wave generated by the ICME itself (see, e.g., Richardson & Cane 2010; Kilpua et al. 2017b). This shock is followed by the sheath region, within which it is possible to observe many important plasma phenomena, such as turbulence and magnetic

^{*} These authors contributed equally to this work.

reconnection, according to the plasma β value (Gosling & McComas 1987; Rouillard 2011; Lapenta et al. 2020). The last part of an ICME passing a satellite instrument can be the Magnetic Cloud (MC) (Burlaga et al. 1981; Klein & Burlaga 1982). The presence of a MC is indicated by an enhancement of the magnetic field strength, with a smooth rotation of the magnetic field direction over a large angle in about one day, and by a decrease in proton temperature and plasma β . We note that only 50% to 75% of the ICMEs drive a shock near 1 au (Salman et al. 2020), while a larger proportion of ICMEs have a sheath region, even in the absence of a shock.

In this work, we focus on the magnetic structures that characterise the evolution of ICMEs at the Lagrangian point L1. In particular, we analyse one event from the catalogue of MCs presented in Al-Haddad et al. (2018), within which the authors compared different techniques of ICME fitting and reconstruction in order to understand which is the most suitable for the selected event. The aim of this paper is different. We want to understand the full chain of events from L1 all the way back to the Sun. One-to-one linkage of in situ detected ICMEs and CMEs in the corona is important, but such linkage is not easy to establish, as there is often ambiguity, especially during or near solar maximum.

In forecasting, we need to determine which type of CME (e.g. halo, partial halo, fast CME) with which solar origin (e.g. near the centre of the solar disc or limb) can produce a geoeffective event. For the purpose of our study, we chose the geoeffective MC of 28 June 2013 that is included in the MC list of Al-Haddad et al. (2018) with the objective of identifying its solar source (CME and active region). To confirm the source of this MC, we tested the multiple CMEs occurring within a five-day time window prior to the arrival of the MC at L1. After describing the data and catalogues that we used (Sect. 2), we present an in-depth analysis of the in situ signatures and their possible solar sources (Sect. 3). After constraining the kinetic parameters for all the possible CMEs, we analyse their propagation through the heliosphere in Sect. 4. We compute the 3D data-driven MHD heliospheric solar wind and model the evolution of the CMEs, individually and all together, using the cone model in the numerical simulation called European Heliospheric FORecasting Information Asset (EUHFORIA; Pomoell & Poedts 2018; Scolini et al. 2019; Poedts et al. 2020). In Sect. 5, we conclude that the CME responsible for the ICME (or MC) registered at L1 on 28 June is a low-speed partial-halo CME. This CME does not encounter any major feature during its transit to 1 au. It propagates towards Earth at an almost constant speed, being advected towards 1 au by the ambient solar wind.

2. Data and model

2.1. Data

The Sun is constantly being imaged remotely in many different wavelengths and by different instruments (both ground based and space borne). With these images, coronal holes, active regions, CMEs, solar flares, and other structures and phenomena that are important for space weather can be identified. For this work, we used the extreme ultraviolet (EUV) observations from the Atmospheric Imaging Assembly (AIA; Lemen et al. 2012) aboard the Solar Dynamics Observatory (SDO; Pesnell et al. 2012). With these observations, we located the position of the source regions of the CMEs that might be responsible for the selected MC. Coronal holes present on the Sun can be detected using the AIA 19.3 nm channel, but no large coro-

nal holes were detected during our observations. Signatures of the eruption were detected using the AIA 30.4 nm channel. We also analysed data from the Helioseismic and Magnetic Imager (HMI; Scherrer et al. 2012) for further insight into the magnetic configuration of the active regions. Furthermore, H- α spectroheliograms from the Paris-Meudon observatory were used to analyse the filaments and prominences that were present on the solar disc at the time of the eruption. In addition, coronagraph white-light images were analysed and used for determining the main direction of propagation of the CMEs, and (if necessary) for constraining the CME geometric and kinematic parameters in order to include them in the simulation model. These were taken from COR2-A and B (SECCHI; Howard et al. 2008) aboard the Solar TErrestrial RElations Observatory (STEREO; Kaiser et al. 2008) and by the Large Angle Spectroscopic Observatory (LASCO; Brueckner et al. 1995), aboard SOHO (SOHO; Domingo et al. 1995).

When CMEs are expelled from the solar atmosphere, they start travelling through the heliosphere. Upon reaching and passing by measuring devices aboard different spacecraft, the plasma parameters being measured are affected, and one can analyse the main characteristics of ICMEs from these observations. To identify the ICMEs that reached Earth's position, we used in situ data obtained from the Advanced Explorer Composition (ACE) spacecraft (Stone et al. 1998; Chiu et al. 1998) located at the L1 point. The local Interplanetary Magnetic Field (IMF) direction and magnitude were measured at a time cadence of 4 min by the MAG instrument (Smith et al. 1998). The solar wind speed and density data were measured with a cadence of 92 s by the Solar Wind Electron, Proton, and Alpha Monitor experiment (SWEPAM; McComas et al. 1998). After the identification process, in situ data were used in a further step as a validation of the model's output (see the following section for a description of the model).

Investigating CMEs and ICMEs together with their effects at Earth is one of the priorities of space weather research. Numerous studies have focused on quantifying ICME effects at Earth, such as their effect on the geomagnetic indexes (Menvielle et al. 2010), effects on ionospheric conditions (Greenwald et al. 1995; Menvielle et al. 2007), and effects on galactic cosmic rays (Masías-Meza et al. 2016). In an effort to standardise the ICMEs that are measured in the near-Earth environment, several ICME catalogues have been developed. Each catalogue focuses on different effects of the CMEs and ICMEs. For this work, we used the SOHO LASCO CME catalogue¹ to identify the corresponding solar sources. This catalogue contains a list of CMEs detected between 1996 and 2022 by the SOHO/LASCO suite (SOHO; Brueckner et al. 1995). It has been generated using many studies, such as (e.g. St. Cyr et al. 2000; Gopalswamy et al. 2004, 2009; Yashiro et al. 2004, 2008), and it is regularly updated. The catalogue provides important CME information and characteristics, including the date and time of the first appearance in the LASCO/C2 field of view, the central angle position, CME speed (obtained using different methods), sky-plane width, and mass and kinetic energy, among others. Moreover, links to additional and complementary information about the CMEs are made available in this catalogue. It is also possible to extrapolate movies from different coronagraphs made by different missions, such as STEREO. The catalogue also provides composite plots that help identify the CMEs and flares associated with specific SEP events or the CMEs responsible for certain intense geomagnetic storms.

https://cdaw.gsfc.nasa.gov/CME_list/

Another very detailed catalogue focused on ICMEs is the Richardson and Cane list². In Richardson & Cane (2010), the authors catalogued over 300 near-Earth events associated with CME events that occurred from 1996 onwards. The authors used measurements of the solar wind and its charge state to identify the ICMEs and to summarise their properties in this list. This catalogue has been continuously expanded in order to cover similar events until 2022, and it is still regularly updated. Richardson and Cane's list provides information similar to the SOHO LASCO CME catalogue, as they combine a number of available data sets and try to assess when an ICME is probably present in the near-Earth solar wind. This list is mostly focused on the ICME characteristics as measured at 1 au and their geoeffectiveness, so disturbance time intervals plus geomagnetic indices are included. It also includes the start and end times of the ICME and the associated MC (if any). Recently, the catalogue of George Mason University (GMU catalogue) has proposed a chain of events between the Sun and the Earth for selected events and years³. Our event belongs to this list. The MC is very well defined, but its solar source is not well defined. In the five-day time window of possible CMEs, many CMEs were observed. It is generally very difficult to make such a chain (Bocchialini et al. 2018), and it is important to test if the proposed CME is travelling in the solar wind with no interaction with other CME or heliospheric structures.

2.2. Model: EUHFORIA

In order to model the possible CME event, we use the EUropean Heliospheric FOrecast Information Asset (EUHFO-RIA; Pomoell & Poedts 2018) which is one of the current stateof-the-art heliospheric forecasting models. In fact, EUHFORIA comprises two models. First, a data-driven coronal model that uses synoptic magnetograms as input and computes the plasma characteristics using the empirical Wang-Sheeley-Arge model (WSA; Arge et al. 2003) at 0.1 au or $21.5 R_{\odot}$ (solar radii). Then, the output of the coronal model is used as the inner boundary condition for the heliospheric wind and CME evolution model. This part solves the 3D time-dependent ideal MHD equations in the Heliocentric Earth EQuatorial (HEEQ) system in order to get the background solar wind at the time the CME occurred. Last, several CME models are implemented into EUHFORIA, such as the cone model (Xie et al. 2004), a linear force-free spheromak model (Kataoka et al. 2009, Verbeke et al. 2019), and the Fri3D model (Isavnin 2016; Maharana et al. 2022). The linear forcefree spheromak model will not be used in this study, as we suspect that the CME impact is a glancing blow and the spheromak model is known to be less useful in such cases (Maharana et al. 2023). As a matter of fact, the spheromak model provides a good approximation to the CME internal magnetic field configuration when the nose of the CME hits the observer. Flank encounters, however, are not well reproduced with a spheromak CME, and even can miss the observer, as the CME-driven shock structure that this model generates, expands less when travelling through the heliosphere in comparison to the cone model. Moreover, the focus of this study is not to reproduce the internal magnetic structure of the MC, but to highlight the importance of selecting the proper solar source. If we aimed at reproducing the magnetic structure, the Fri3D model would provide a more realistic

approach, but the main drawback of this model is the substantial CPU time requirements. As we are aiming at comparing the arrival times of several CME candidates, it is not sensible and not necessary to use this model to perform multiple simulations.

For the present study, we used the simpler cone CME model, which injects at the inner boundary (at 0.1 au), a hydrodynamic pulse without an intrinsic magnetic field. Only 7 parameters are needed for a cone CME, including the time of insertion at $21.5 R_s$ (= 0.1 au), the latitude and longitude of the propagation direction of the cone, the angular half-width, the speed of insertion, the plasma density, and the temperature. The first five parameters for the selected CME event were obtained using the STEREO CME Analysis Tool (StereoCAT; Mays et al. 2015), developed by the Community Coordinated Modeling Center (CCMC). Temperature and density for the CME model were left unchanged from the default values of $0.8 \, \text{MK}$ and $10^{-18} \, \text{kg m}^{-3}$. The cone model, although it does not possess an intrinsic magnetic field, has been extensively used as it is an accurate model for predicting the time of arrival of CME-driven shocks with EUHFORIA (e.g. Scolini et al. 2018, Palmerio et al. 2019; Kilpua et al. 2019).

3. Event analysis

3.1. In situ measurements

Figure 1 shows interplanetary magnetic field and plasma measurements by the ACE spacecraft near Earth around the passage of the MC of 27 June 2013. In this figure we present, from top to bottom, the magnetic field strength (panel a); the three components of the magnetic field in the Geocentrical Solar Ecliptic (GSE) coordinate system (B_x , B_y , and B_z in panels b, c, and d, respectively), as measured by ACE/MAG; and the solar wind density, bulk speed, temperature, and pressure in the panels e through h, as measured by ACE/SWEPAM.

The in situ measurements before the arrival of the event show a very stable IMF in all three magnetic field components and a low density together with a decreasing tendency in the solar wind speed. The temperature and pressure also registered a stable behaviour prior to the arrival of the ICME. On 27 June 2013, at around 13:00 UT, a sudden enhancement in the oscillation rate of the IMF components and a jump in all other solar wind plasma parameters was registered, indicating the arrival of a CME-driven shock. This can be seen in Fig. 1, marked by the vertical red dashed line. An increase of ~50 km s⁻¹ in solar wind velocity (panel f) was registered upon the arrival of the shock. The solar wind temperature and pressure (panels g and h, respectively) sharply increased and remained at elevated levels throughout the duration of the sheath region. The magnetic field components maintained this behaviour for about 12 h. In the same period, the density gradually increased, while the velocity, temperature, and pressure had a decreasing trend. This corresponds to the passage of the sheath region of the ICME.

After the passage of the sheath, we observed that the associated MC had a smooth rotation in all components of the IMF, a higher magnetic field strength, and a lower temperature. The MC passage started at 02:23 UT on 28 June and lasted for about 33 h, as listed in Al-Haddad et al. (2018). The starting and ending times of the MC are marked with vertical green dashed lines in Fig. 1. A rotation from positive to negative values in B_z was observed, while B_y showed a rotation from negative values towards positive values, starting at \sim 10 nT and finishing the period at \sim 10 nT. On the other hand, B_x began the period close to 0 nT and increased slightly until 29 June at 03:00 UT, when it

https://izw1.caltech.edu/ACE/ASC/DATA/level3/ icmetable2.htm

http://solar.gmu.edu/heliophysics/index.php/ ICME-CME-SSS_catalog

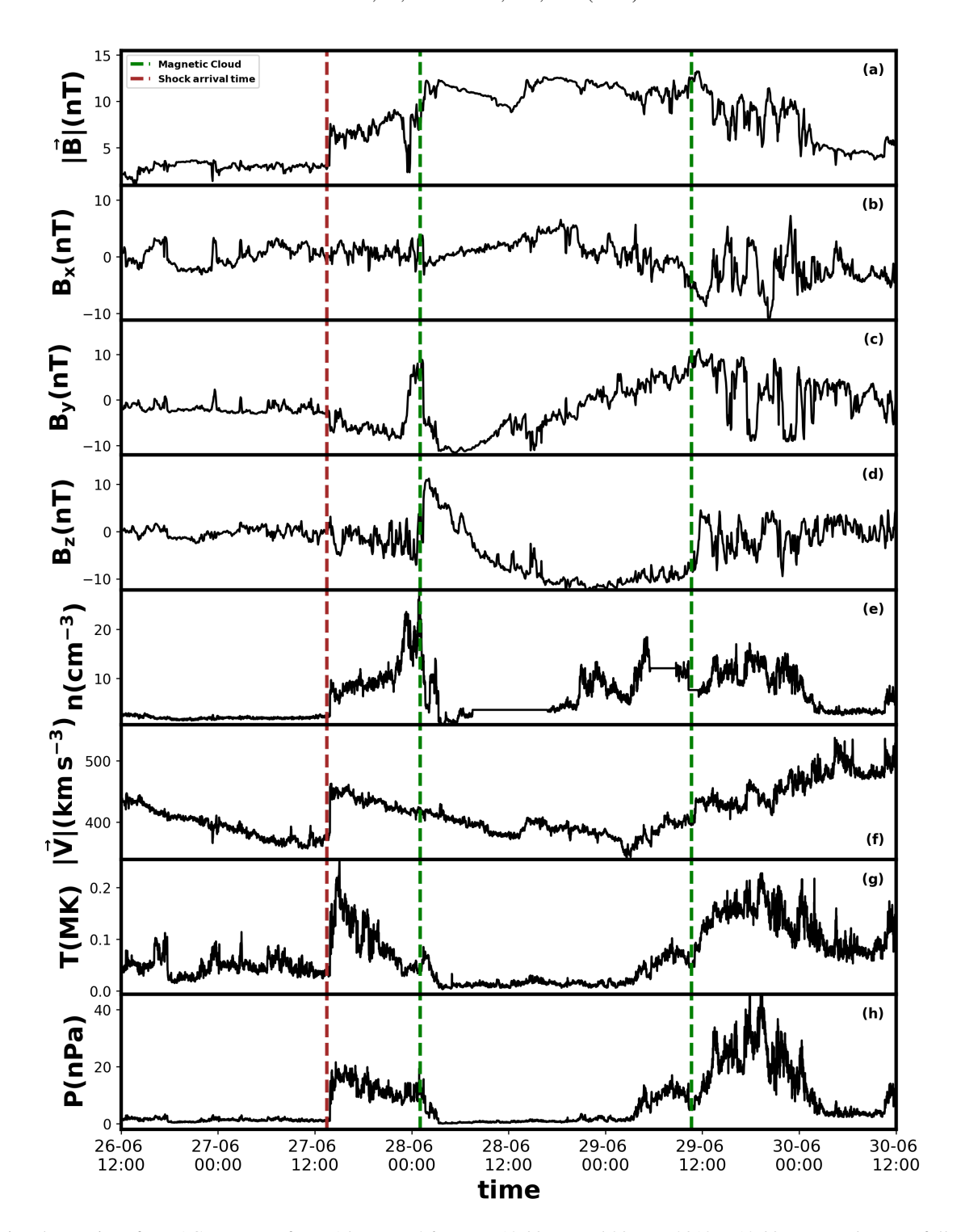


Fig. 1. In situ observations from ACE spacecraft at L1 between 26 June at 12:00 UT and 30 June 2013 at 12:00 UT. Panels are as follows: profiles of the magnetic field magnitude (panel a), the three components (B_x , B_y , and B_z in panels b, c, and d, respectively), density (panel e), bulk speed (panel f), temperature (panel g), and gas pressure (panel h). The red vertical dashed line indicates the shock arrival time, and the two green vertical dashed lines mark the start and the end of the MC.

started decreasing until it reached the minimum of ~ -5 nT at the end of the MC passage. The solar wind speed had a decreasing tendency until 29 June at 03:00 UT, when it reversed its trend and started increasing. The temperature and pressure remained more or less stable and at low values until this shift in the B_x and the reversal in the solar wind speed tendency. From that point onwards, the temperature and pressure increased until the end of the MC.

3.2. Coronal mass ejections and solar sources

In a time window of five days before the passage of the MC at L1, six CMEs were detected. Our aim was to test with EUHFORIA whether the CME proposed by the GMU catalogue is the driver of the MC when we model its propagation in a realistic solar wind. We used the StereoCAT tool to obtain the parameters needed for the simulation. We compiled the information

Table 1. Six CME candidates that are possibly related to the MC of 28 June 2013.

	Date (D/M/Y)	Time (UT)	Width (°)	Speed (km s ⁻¹)
CME 1	23/06/2013	02:36	73	261
CME 2	23/06/2013	21:24	101	339
CME 3	23/06/2013	22:36	174	174
CME 4	24/06/2013	04:00	360	709
CME 5	25/06/2013	08:24	92	562
CME 6	25/06/2013	11:12	360	349

Notes. Candidates are detected by the ACE spacecraft, defined by the date and time of their first appearance in LASCO C2, their angular width, their linear speed in C2 (from the CDAW catalogue). CME3 is the proposed CME in the GMU catalogue. Bold indicates the CME event responsible for the signal seen by the spacecraft.

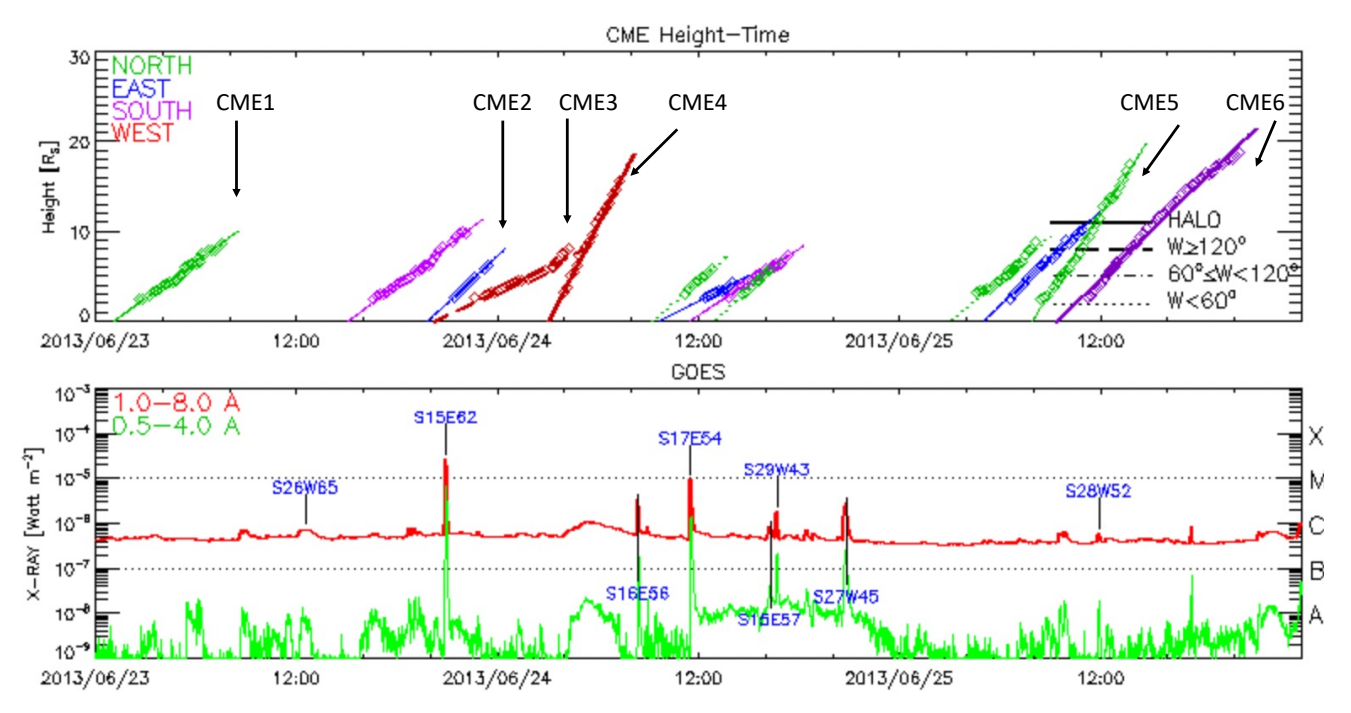


Fig. 2. CME characteristics. The top panel shows the height-time plots, and the six CMEs studied in this article are marked with arrows. The colours code the main CME direction (see left inset), while the type of lines codes the CME apparent angular extension (see right inset). The bottom panel shows the GOES X-ray flux in two wavelengths with the solar source coordinates of the identified events. The time range is from 23 June 00:00 UT to 25 June 24:00 UT (adapted from the CDAW catalogue).

from the different CME catalogues and used images from the different spacecraft described in Sect. 2.

Six candidate CMEs are reported in the catalogues in a time window of three to five days prior to the arrival of the MC at Earth (Table 1 and Fig. 2). To compare the spacecraft data to the simulation results, we analysed each CME and its characteristics (speed, direction of propagation, and solar source, when possible).

The height-time profiles for the detected CMEs are presented in Fig. 2. The CME events 1 through 6 from Table 1 are indicated with black arrows. Here, the direction of propagation of the CMEs is colour-coded following the legend in the top-left inset of the top panel. The angular width in the plane-of-sky is identified with the line type (see the legend in the bottom-right inset of the top panel). Both CME 1 and CME 5 have a northward propagation direction, and both have an angular width between 60 and 120 degrees. The only selected event that has an eastward propagation direction is CME 2, and its angular width is between 60° and 120°. Regarding CME 6, it is registered as a halo CME with a southward propagation direction, and it is traced up to 22 solar radii. Finally, CME 3 and CME 4 have a westward prop-

agation direction. Notably, CME 3 shows the lowest speed of all six events and has an angular width of over 120°, while CME 4 is registered as a halo event. The bottom panel of Fig. 2 shows the GOES X-ray flux in two different wavelengths. The blue letters indicate the origin location of the registered flares. This period of time was relatively quiet, with only a few short-duration C-class X-ray flares and one M-class flare.

One may think that a full or partial halo CME could be responsible for generating the MC focused on in this study. From the SOHO LASCO CME catalogue, there are two possible candidates that were halo CMEs and erupted from the Sun within this time window of three to five days prior to the arrival of the MC at Earth. The first of these halo CME events (CME 4) was launched from the Sun on 24 June at 04:00 UT. This event was first seen in the LASCO-C2 field of view at 04:00 UT, while in COR2-A and B, it was first seen at 05:09 UT and 05:09 UT, respectively. The speed was estimated to be 709 km s⁻¹. When analysing the AIA 30.4 nm images, however, no clear signature of this event can be seen on the solar disc. When checking the direction of propagation with STEREO-A and STEREO-B together with the position of the spacecraft that captured this

2013-06-23 13:30:00

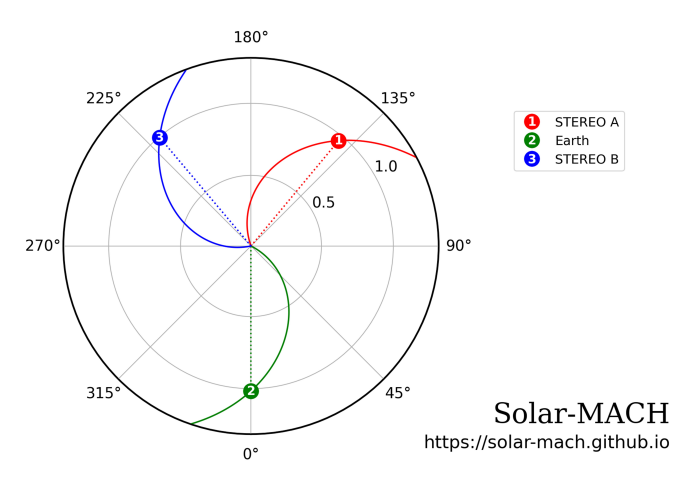


Fig. 3. Spacecraft constellation position on 23 June 2013. The figure was generated using Solar-MACH (Gieseler et al. 2023).

event (shown in Fig. 3), it is evident that the direction of propagation of this event is towards the backside of the Sun. This excludes this halo CME event from being responsible for the magnetic cloud of interest.

The second event we analysed is CME 6. From the SOHO LASCO CME catalogue, this halo CME erupted on 25 June, and it was seen by the LASCO-C2 detector at 11:12 UT with an estimated plane-of-sky speed of 349 km s⁻¹. This CME was also seen by STEREO COR2-A at 11:39 UT and STEREO COR2-B at 11:54 UT. We used the StereoCAT tool to fit this event (see Table 2), but we found the longitude of the propagation direction of the CME to be 175°, which makes it a backside event. The low-speed of this event, together with the direction of propagation, makes CME 6 incompatible with an event that generates the MC of interest at L1 two days later.

Concerning the other four candidates, CME 2 and CME 3 (Fig. 2) were initiated in fast succession. Figure 4 shows the HMI magnetogram (panel a), AIA 17.1 nm (panel b), and 30.4 nm (panel c) for 23 June at 13:29 UT prior to the eruption of CME 2 and CME 3. The CME 1 event was seen approximately 20 h before CME 2 (as reported in the CDAW catalogue shown in Table 2). The light-pink arrow points at the approximate location of the source of CME 1. The white arrow points at the approximate position of AR 11778, the source of CME 2. The yellow arrow and circle point at the position of the source of CME 3, which does not correspond to any reported active region. The CME 5 event was seen 10 h after CME 3, with an angular width close to 90. This event was seen propagating northward (see Fig. 2).

From the Richardson and Cane list, the magnetic cloud of interest is reported to have an associated CME, which is not seen as a halo CME. It was reported that the magnetic cloud leads to a geoeffective magnetic storm with a Dst index of –102 nT, which is already in the class of intense events (Zhang et al. 2007). The CME 1 event erupted around 20 h before CME 2 and CME 3, but the speed at which it propagated was very slow. This caused the event to still be present in all available (e.g. all coronagraph images form the period we study) coronagraph images (see Fig. 5). The direction of propagation of CME 1 is very apparent and has a large northward component, which makes it incompatible with a hit at Earth. Analysing images from SDO/AIA 17.1 nm, there is a thin filament structure positioned at approx-

Table 2. StereoCAT fitting parameters chosen for the CME candidates.

	φ (°)	θ (°)	α (°)	$V_{\rm cme} ({\rm km s}^{-1})$	Passes at 21 R _☉
CME 1	-60	48	17	224	2013/06/23 18:30
CME 2	-62	-15	20	489	2013/06/24 06:01
CME 3	14	14	27	391	2013/06/24 09:17
CME 4	175	-15	56	844	2013/06/24 07:47
CME 5	-41	61	22	487	2013/06/25 15:53
CME 6	175	-21	38	620	2013/06/25 16:48

Notes. The terms are as follows: $\phi(^{\circ})$ is the heliographic longitude; $\theta(^{\circ})$ is the heliographic latitude, both measured in the HEEQ system (Heliocentric Earth Equatorial); $\alpha(^{\circ})$ is the angle between the legs; $V_{\rm cme}({\rm km\,s^{-1}})$ is the CME speed propagation; and 'Passes at 21 R_{\odot} ' indicates the time when the CME reaches 21.5 R_{\odot} , according to the model parameters. Bold indicates the CME event responsible for the signal seen by the spacecraft.

imately N35 E60 that erupts very slowly into a streamer-like structure. In contrast, CME 2 and CME 3 are much more aligned with the ecliptic plane, making them the more suitable events to keep analysing. The brightness of CME 1 in the images is much higher than the brightness of the two other events. This is due to the combination of the streamer and the very slow speed of eruption of CME 1, which enhances the brightness in the white-light images. This means that the analysis of the coronagraph images requires significantly more effort. In Fig. 2, bottom panel, we observed a GOES X-ray M2.9 class flare at around 22:00 UT originating at S15 E62, close to the active region NOAA AR 11778 positioned at S15 E47. This is close in time with CME 2 and CME 3. The CME 2 event was reported to have erupted close to this position with a speed of 339 km s⁻¹. The main direction of propagation is towards the southeast, and due to the position of the spacecraft and the high brightness of CME 1, it cannot be clearly seen in COR2-B. The CME 3 event erupted from a small active region (though not classified as such by NOAA) positioned at N14 W14 at the time of the eruption. marked in Fig. 4 with a yellow arrow and circle. The CME 3 event appears to be the best candidate (Table 1) for explaining the studied MC passage at L1. This confirms the proposed CME in the Sun-Earth chain of the GMU catalogue.

In Fig. 5, we show the coronagraph white light observations by COR2-A and COR2-B for 23 June at 23:39 UT aboard STEREO A and B spacecraft, respectively, and the running difference images from LASCO-C2, aboard SOHO, at 23:36 UT. It is clear from the coronagraph running difference images that it is not easy to select the CME associated with the event detected by the spacecraft positioned at L1.

From COR2-A (Fig. 5a), it is possible to distinguish the presence of CME 1 in the northern region of the image, CME 2 in the southwestern region of the image, and the faint CME 3 in the eastern flank. Due to its faintness and the high brightness from CME 1, CME 2 is neither clear nor easy to see. In Fig. 5b field of view, we can only observe CME 1. This is due to the faint nature of both CMEs (e.g. CME 2 and CME 3) and their direction of propagation with respect to STEREO-B. As seen from LASCO-C2 (Fig. 5c), CME 1 is barely visible; CME 2 appears on the south-eastern side of the figure; and on the north-western side, it is possible to see the presence of a faint CME (CME 3), similar to what we can be seen in Fig. 5a. For all cases, the detection of the main suspect CMEs is complicated by the fast and wide CME 1, which is seen propagating northward.

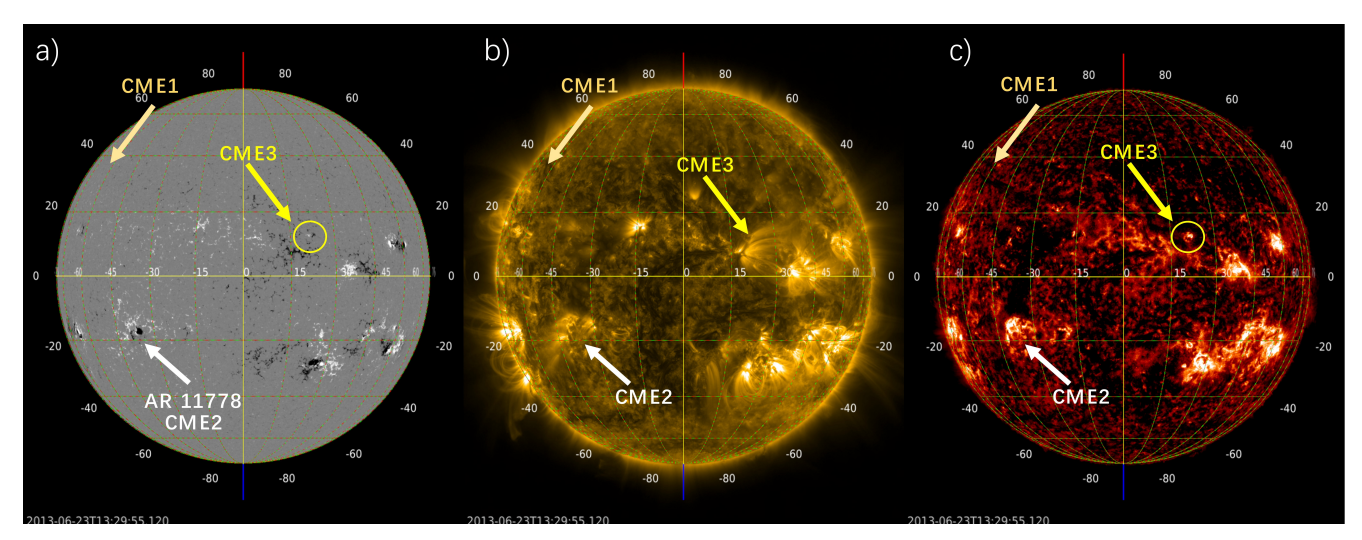


Fig. 4. Solar disc images taken from SDO. The panels are as follows: HMI magnetogram (panel a) together with the AIA 17.1 nm and AIA 30.4 nm images (panel b and c, respectively) on 23 June 2013 at 13:29 UT. The light-pink arrow shows the approximate position of the source of CME 1. The white arrow shows the position of NOAA AR 11778, origin of CME 2, while the origin of CME 3 is marked with a yellow arrow and circle. The CME 3 source region corresponds to a tiny emerging flux at the edge of a filament channel.

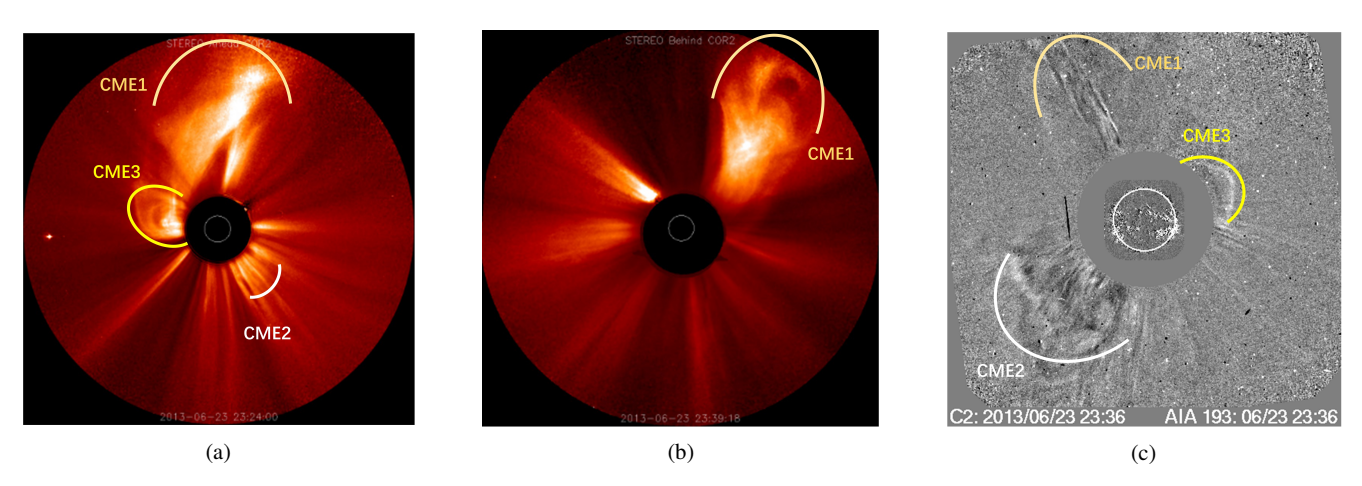


Fig. 5. White-light coronagraph images taken from STEREO/SECCHI/COR2-A and COR2-B (panels a and b, respectively) on 23 June at 23:39 UT. Panel c shows the SOHO/LASCO/C2 running difference white light coronagraph observation at 23:36 UT for the same day. Highlighted using light pink, white, and yellow are CME 1, CME 2, and CME 3, respectively. No clear signatures of CME 2 and CME 3 are present in STEREO/SECCHI/COR2-B.

3.3. Parameters of the coronal mass ejections

In order to reproduce the CME observed by the coronagraphs, we fit the events with the help of the StereoCAT tool⁴. StereoCAT is an online tool designed for space weather forecasts and research, and it allows users to obtain the kinematic properties of CMEs. The parameters derived with this tool (latitude (ϕ) , longitude (θ) , half angle (α) , speed of the CME $(V_{\rm cme})$, and passage time at 21 solar radii (R_{\odot})) can be used as input parameters for a broad range of CME propagation models. The parameters obtained for the CMEs we analysed are reported in Table 2.

The parameters of the StereoCAT fitting show that CME 3 propagated towards Earth's direction with a low velocity, which is comparable with the background solar wind speed (400 km s⁻¹) measured at Earth prior to the event (see Fig. 1). This confirms the coordinates of the source that we identified. From our analysis and fittings, it emerged that the CME responsible for the event detected by ACE is most probably CME 3.

However, in order to verify which halo and non-halo CMEs (Table 1) could be responsible for the MC observed at Earth, we used EUHFORIA to model their propagation through the interplanetary medium (see Sect. 4).

4. EUHFORIA simulations

Before running the EUHFORIA simulation, a coronal model has to be computed for the day the CME started its journey in the corona (until 0.1 au). EUHFORIA's coronal model is data driven (see Sect. 2). To run the simulation, we selected the magnetogram of 22 June 2013 at 22:36 UT as provided by the Global Oscillation Network Group and Air Force Data Assimilative Photospheric Flux Transport (GONG-ADAPT). The result for the solar wind is presented in Fig. 6. We found a relatively good agreement between simulations and in situ measurements when comparing the solar wind density and speed between 25 June at 00:00 UT and 27 June at 12:00 UT, just before the arrival of the CME. Considering the list of possible CMEs shown in Table 1,

⁴ Available online at https://ccmc.gsfc.nasa.gov/analysis/ stereo/

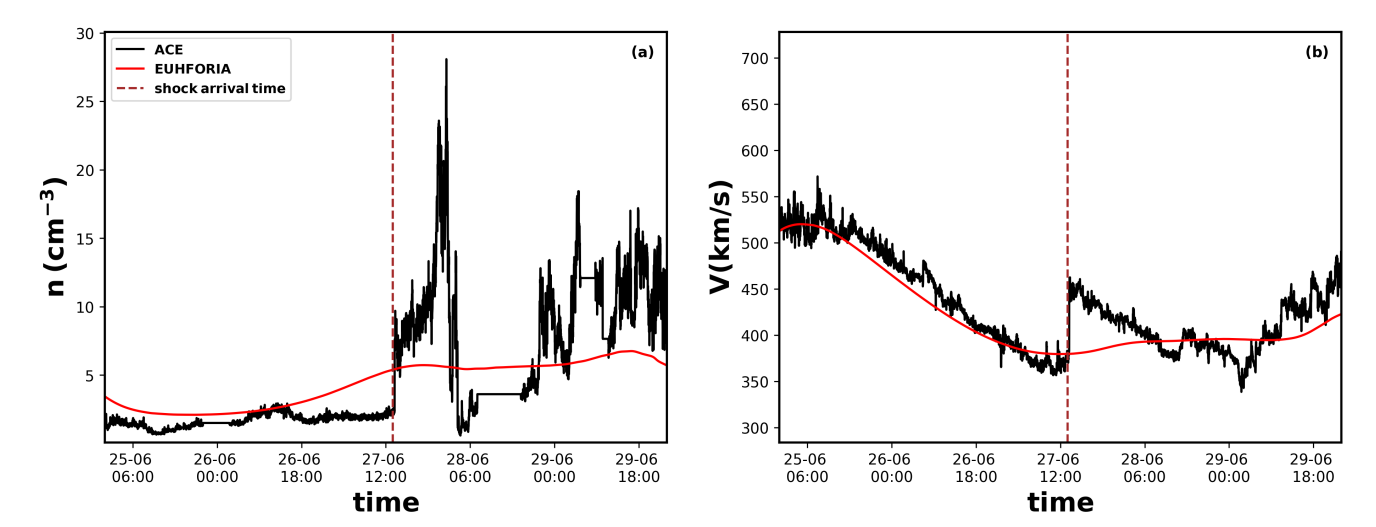


Fig. 6. 'Best' EUHFORIA simulation results for the background solar wind computed at L1 (red curves) between 25 and 30 June 2013 compared with in situ measurements at L1 (black curves); The left panel shows the density, and the right panel shows the solar wind speed. The best simulation was chosen by comparing several simulations obtained after slightly varying the parameters of EUHFORIA's coronal model. We note the very good fit of the solar wind speed before the shock time preceding the ICME at L1 (vertical dashed line).

we tested each of them individually to see if they could reach the Earth.

As anticipated by our analysis from observations and fittings and considering the list of six possible CMEs shown in Table 1, we began our investigation by modelling each CME separately to obtain an initial assessment as to which are capable of impacting the Earth.

To obtain a more accurate overall representation of the heliosphere, which is known to experience preconditioning due to the passage of solar transients (e.g. Temmer et al. 2017; Desai et al. 2020) and to take advantage of the ease of using the computationally efficient cone model, we also ran a simulation that included all six CMEs. The results are shown in Figs. 7 and 8. The simulations were made using a 2 degrees angular resolution in the longitudinal and latitudinal direction and a radial resolution of ~0.0039, with the domain extending up to 2 au. Two snapshots of the EUHFORIA simulation with all CMEs injected are shown in Fig. 7. The top panels correspond to the time when CME 3 is at ~ 0.5 au. The bottom panels correspond to the time when CME 3 is at 1 au (affecting Earth). The left panels show the number density. The right panels show the simulated radial solar wind speed. Each panel is composed of an equatorial slice (the left panel) and a meridional slice that includes the Earth (the right panel). All the panels include the position of STEREO-A and B, as well as the position of the planets in the inner heliosphere. Considering the time of insertion of CME 3 and the simulated time of arrival at Earth's position, the transit time of this CME to 1 au is about four days. This is expected since the StereoCAT fitting results show a velocity comparable to the ambient solar wind velocity into which the CME is injected. The CME 1 event is not marked in any of the snapshots due to its reduced size and slow propagation speed. Moreover, as CME 2 was injected at a later time and propagated in a similar direction, the signature of CME 1 was lost. The CME 4 and CME 6 events propagate towards the back of the Sun, as seen from the individual runs and from the results presented in Table 1. Both CMEs could have been discarded from the possible CMEs that caused the MC. In contrast, a small component of CME 2's propagation direction goes into CME 3, but no clear interaction was observed at the Earth's position, as shown in Fig. 8. Finally, CME 5 is not marked in the snapshots of Fig. 7, as its latitude of insertion exceeds the simulated domain latitude. Additionally, this CME's angular width would not be enough to affect Earth nor CME 3's direction of propagation.

In Fig. 8, we present the comparison between the EUHFORIA simulations and ACE data. From top to bottom, the panels show the solar wind density, speed, temperature, and pressure. The black line represents in situ measurements. The red solid line represents the EUHFORIA results for the simulation where all the CMEs are injected, while the blue dashed line corresponds to the simulation where only CME 3 is injected. In each panel, the red-shaded area was generated using the simulated data with a virtual spacecraft positioned at $\pm 5^{\circ}$ with respect to Earth in both latitude and longitude. This mesh of virtual spacecraft allowed us to recover the time series at other positions, which can be helpful in the case of having some unaccounted error in the kinetic parameters when injecting the CME in the heliospheric domain.

When comparing the two simulations, we found no difference between them in any of the variables presented. Furthermore, there is a good agreement between EUHFORIA simulations and in situ observations at 1 au. The two datasets do show differences, as no simulation is 100% perfect, but it is indeed good to point out that the modelling results are very consistent with ACE data (especially in the arrival time and speed of CME 3). These results are a further confirmation that CME 3 is the only CME affecting the Earth at the time of interest. The strong enhancement registered in the simulated density (panel a of Fig. 8) is in good agreement with the one registered in the in situ data, with some initial overestimation after the shock passage (marked with a vertical dashed line). After the sheath region passed over the observer, the MC started affecting it (first green vertical dashed line). A decrease in density was registered earlier in the simulations than in the ACE data. This underestimation of density affects the speed, from which it results in a slight overestimation of the bulk solar wind speed (panel b of Fig. 8) inside the magnetic cloud. The simulated temperature (panel c of Fig. 8) is in excellent agreement with the observed data. The simulated temperature profiles rose sharply, though slightly earlier than the in situ data. This underestimation of the density

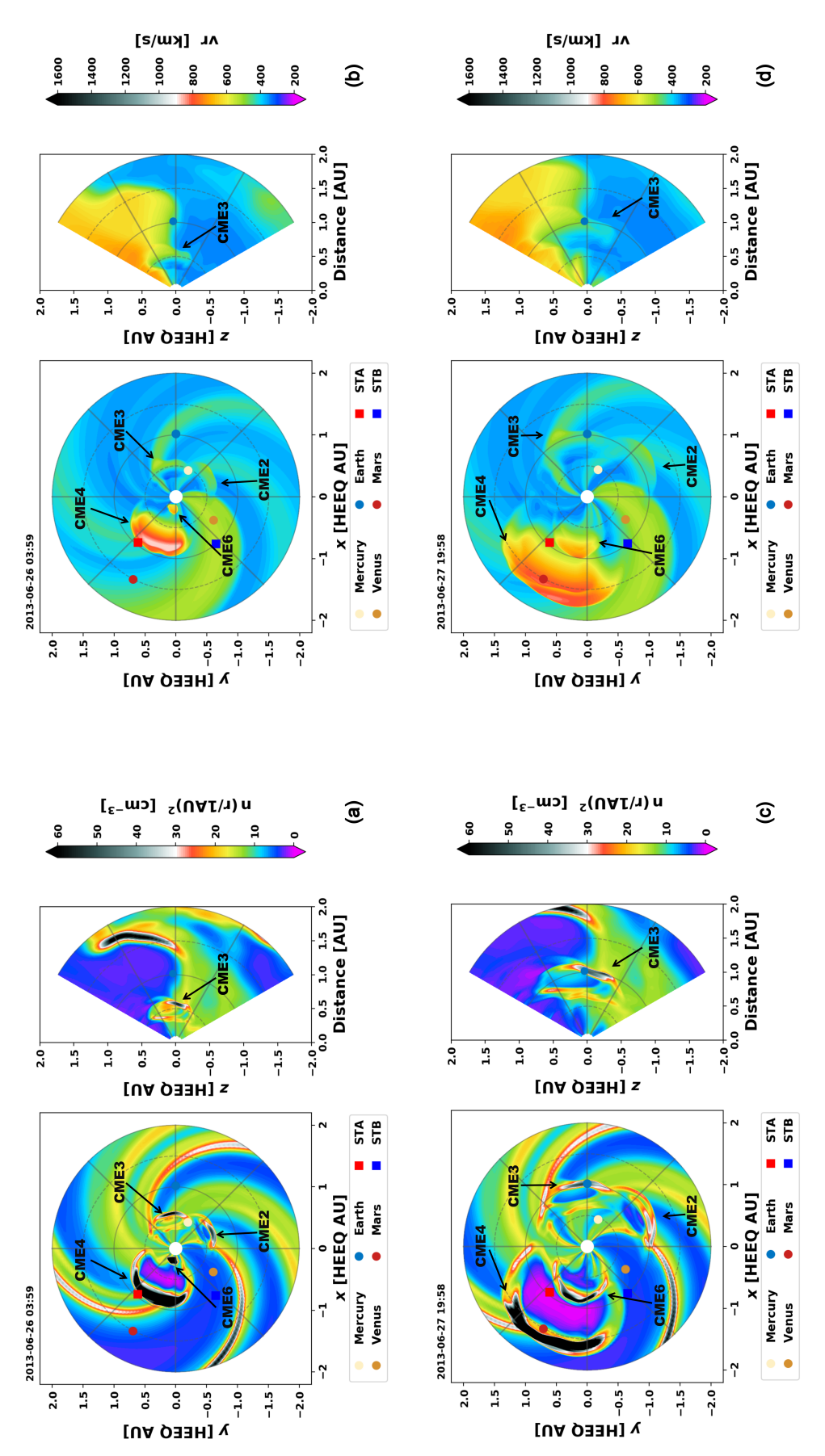


Fig. 7. Overview of EUHFORIA results for the simulations where all the CMEs are simulated using the cone model. Scaled plasma number density (left panels) and radial velocity (right panels). The top panels correspond to 26 June at 03:59 UT, and the bottom panels correspond to 27 June at 19:58 UT. Each of the panels is composed of an equatorial slice of the simulation (left) and a meridional slice that contains Earth (right). The position of the ICMEs (CMEs) is indicated with black arrows and their associated name. As explained in the text, CME 1 is too weak, and CME 5 is out of the domain; neither of them are visible in this figure.

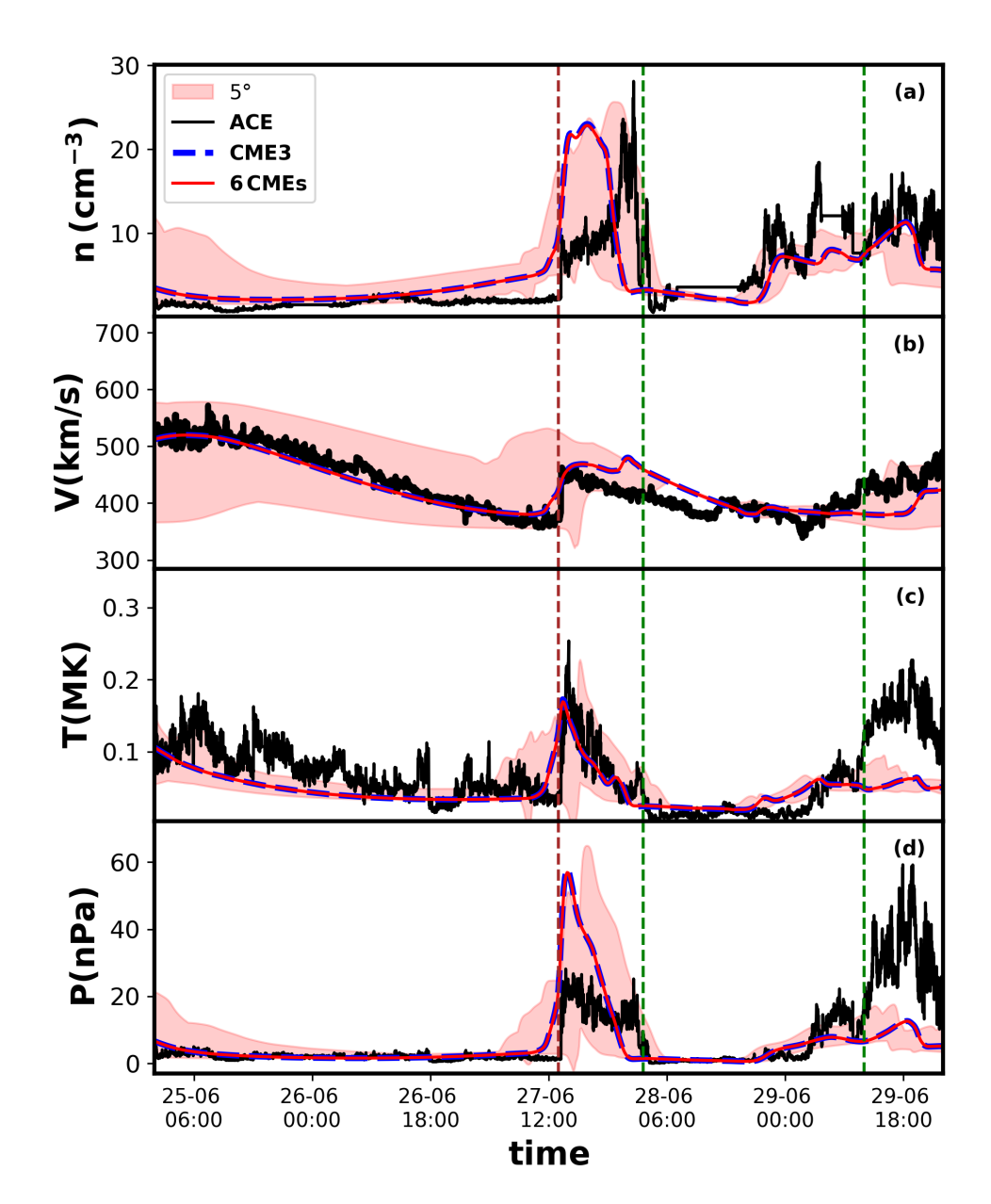


Fig. 8. Comparison between EUHFORIA simulation results at 1 au and ACE spacecraft data. From the top panel to the bottom panel, we present the number density, solar wind bulk speed, temperature, and pressure of the solar wind. The spacecraft data are indicated with a solid black line. Results for the EUHFORIA simulation where all the CMEs are injected are indicated with a solid red line, while the EUHFORIA simulation results where only CME 3 was injected are shown with a dashed blue line. The shaded area represents the combination of the results of the plasma parameters obtained from virtual spacecraft placed at $\pm 5^{\circ}$ in longitude and/or latitude from Earth for the run with all the CMEs.

and pressure is due to the model's resolution. A very similar behaviour to the temperature was observed for the simulated pressure (panel d of Fig. 8) but with an overestimation at the beginning of the sheath region due to the dependence of the simulated pressure on temperature and density.

Very often, differences observed between in situ measurements and simulation results are attributed to interactions with (and preconditioning by) the structured solar wind and/or solar transients, such as other CMEs and High-Speed Streams (HSSs) (e.g. Shiota & Kataoka 2016; Török et al. 2018; Scolini et al. 2019; Palmerio et al. 2022). Interactions between CMEs and HSSs and their preceding stream interaction regions, as well as other CMEs, can result in accelerations, decelerations, rotations, deflections, deformations, or even increased geoeffectiveness (Heinemann et al. 2019; Liu et al. 2019; Scolini et al.

2020; Winslow et al. 2021; Kay et al. 2022). In our case, the agreement is good enough to conclude that we did not encounter such interactions, at least along the Sun-Earth line.

5. Summary and conclusions

This work focused on the study of a particular case of an MC observed at L1 on 28 June 2013 at 02:23 UT. This period of time is close to the maximum of solar cycle 24. It is well known that during a solar maximum, the frequency of CMEs increases in comparison to the solar minimum. Therefore, there were six possible candidates in a time window of five days prior to the MC: two halo CMEs (CME 4 on 24 June at 04:00 UT and CME 6 on 25 June at 11:12 UT) and four partial halos and low-speed CMEs.

From the six CMEs, the ones designated in this work as CME 2 and CME 3 were found to be the most probable events responsible for the MC measured at L1 on 28 June. Both events erupted on 23 June at 21:24 UT and 22:36 UT, respectively. We analysed HMI magnetograms, AIA 30.4 nm, and 17.1 nm images just before 22:00 UT and detected some brightenings that helped us determine the position of the source. We identified the possible source of CME 2 in the active region NOAA AR 11778 in the south-east solar disc and the CME 3 source in a tiny bright point close to a filament channel at longitude equal to 15 degrees. The tiny brightening corresponds to an emerging flux at the edge of a filament channel. It is a favourable location for reconnection between emerging flux and open field and for CME.

We used the StereoCAT tool to obtain the CME parameters required by the cone CME model in EUHFORIA, and we performed 3D MHD modelling of the events to further confirm that the CME coming from the north-west (CME 3) was ultimately responsible for the MC. As a first step, we optimised the EUHFORIA background solar wind in order to obtain the most realistic conditions of propagation for the CMEs. Then, they (the CMEs of interest in our study) were injected into the EUHFORIA heliospheric domain. We analysed their propagation in the heliosphere in isolation (separated EUHFORIA simulations) and in conjunction with each other (the six CMEs injected into the same simulation). The latter simulation was performed to evaluate CME propagation in a solar wind as realistically as possible. However, the results obtained from the isolated analysis of CME 3 do not differ from those containing all the CMEs. This is mainly due to the direction of propagation of most of the CMEs analysed: CME 4 and CME 6 propagated towards the backside of the Sun, while the direction of propagation of CME 5 is not close to the Sun-Earth line. Since the two runs (six CMEs and only CME 3) do not show differences between them, we concluded that CME 3 did not experience preconditioning by preceding eruptions along the Sun-Earth line. Furthermore, its origin is outside the simulation's domain, and therefore it was not injected in the heliospheric domain. On the other hand, CME 1 is very narrow and slow. This CME was injected and advected by the ambient solar wind, but as its direction of propagation coincides with the propagation direction of CME 2 (which is faster and wider), there are no clear signatures of this event. The EUHFORIA simulations show that CME 3 is the only one capable of generating the MC passage measured at L1, as the arrival time, velocity, and density increase have been perfectly recovered, as showed in Fig. 8.

The proposed solar source of the GMU catalogue concerns a small plage region (x = 0, y = 14 degrees). We tested this solar source with EUHFORIA and found that the result is slightly better with our solar source in the filament channel focused on a tiny emerging flux at N14 E14, which shows some enhancement of brightening at the time of the CME.

The EUHFORIA tool is very useful for confirming the CME responsible for the observed MC passage. Further improvements to the simulations could be made, as we used the simple cone model in this case. This model does not take into account the internal magnetic structure of the CMEs, and therefore, it is not capable of reproducing the evolution of the different magnetic field components during the propagation of the ICME. The geometric parameters required for the spheromak model can be obtained by using the GCS model (Thernisien 2011). A completely different fit would be required for FRi3D, as it has additional parameters. The main drawback of these two models for this particular case is the need to obtain the necessary magnetic parameters. Due to the weak nature of the event, the applica-

tion of the techniques normally used for larger events would not only prove to be extensive and difficult but would also change the scope of the work presented. Such papers as Maharana et al. (2023) and Scolini et al. (2019) address these calculations, illustrating their complexity. In a future work, we will include a different model of EUHFORIA with the aim of reproducing the MC, such as spheromak or FRi3D (Verbeke et al. 2019; Maharana et al. 2022).

In the present case, the two fast halos that fit with the propagation time did not do it (the longitude and latitude values extrapolated from the fit analysis shows that the two halo CMEs do not propagates towards Earth) in the Sun-Earth direction and did not arrive at Earth. Our statistical analysis based only on fast halo CMEs as candidates in a three-to-five-day time window prior to an MC is ambiguous, especially during solar maximum periods. This confirms the conclusion obtained by Schmieder et al. (2020), whose authors analysed 12 X-ray flares with 12 associated halo CMEs. In that work, the authors concluded that none of the 12 halo CMEs were really geoeffective. One of the CMEs with a source at the central meridian and a fast speed has been tested by EUHFORIA, and due to lateral over expansion, the CME could not be geoeffective (Verbeke et al. 2022). Additional conditions are needed for the geoeffectiveness (Rodriguez et al. 2008, 2009; Echer et al. 2008, 2013; Bein et al. 2011; Bocchialini et al. 2018). In fact, C-class flares accompanied by partial filament eruptions and slow-speed CMEs can be geoeffective (Chandra et al. 2010; Bocchialini et al. 2018). Studies by Zuccarello et al. (2018), Linan et al. (2018, 2020) show the importance of considering the solar source of the CME with its complexity and its excess in magnetic helicity.

We plan to study all the magnetic clouds in the heliosphere listed by Al-Haddad et al. (2018) in order to detect and analyse their solar sources. We believe using a more realistic CME model, other than the cone model used in this work, would also be helpful to better studying and reproducing the evolution of the CME of the Sun. This would also help reproduce the evolution of the magnetic field associated with a CME.

Acknowledgements. The resources and services used in this work were provided by the VSC (Flemish Supercomputer Center), funded by the Research Foundation – Flanders (FWO) and the Flemish Government. N.A. acknowledges support from NSF AGS-1954983 and NASA ECIP 80NSSC21K0463 and 80NSSC22K0349. The research by G.P. acknowledges POR Calabria FSE/FESR 2014-2020 for financial support. S.P. acknowledges support from the European Union's Horizon 2020 research and innovation programme under grant agreement No 870405 (EUHFORIA 2.0) and the ESA project 'Heliospheric modelling techniques' (Contract No. 4000133080/20/NL/CRS). These results were also obtained in the framework of the projects C14/19/089 (C1 project Internal Funds KU Leuven), G.0B58.23N (FWO-Vlaanderen), SIDC Data Exploitation (ESA Prodex-12), and Belspo project B2/191/P1/SWiM. V.C. and F.L. acknowledge support from the Italian MIUR–PRIN Grant No. 2017APKP7T on Circumterrestrial Environment: Impact of Sun-Earth Interaction.

References

Al-Haddad, N., Nieves-Chinchilla, T., Savani, N. P., Lugaz, N., & Roussev, I. I. 2018, Sol. Phys., 293, 73

Arge, C. N., Odstrcil, D., Pizzo, V. J., & Mayer, L. R. 2003, Am. Inst. Phys. Conf. Ser., 679, 190

Bein, B. M., Berkebile-Stoiser, S., Veronig, A. M., et al. 2011, ApJ, 738, 191 Bocchialini, K., Grison, B., Menvielle, M., et al. 2018, Sol. Phys., 293, 75 Brueckner, G., Howard, R., Koomen, M., et al. 1995, Sol. Phys., 162, 357 Brueckner, G. E., Howard, R. A., Koomen, M. J., et al. 1995, Sol. Phys., 162, 357

Burlaga, L., Sittler, E., Mariani, F., & Schwenn, R. 1981, J. Geophys. Res., 86, 6673

Chandra, R., Pariat, E., Schmieder, B., Mandrini, C. H., & Uddin, W. 2010, Sol. Phys., 261, 127

```
Chiu, M., Von-Mehlem, U., Willey, C., et al. 1998, Space Sci. Rev., 86
Davies, E. E., Möstl, C., Owens, M. J., et al. 2021, A&A, 656, A2
Desai, R. T., Zhang, H., Davies, E. E., et al. 2020, Sol. Phys., 295, 130
Domingo, V., Fleck, B., & Poland, A. I. 1995, Sol. Phys., 162, 1
```

- Echer, E., Gonzalez, W. D., Tsurutani, B. T., & Gonzalez, A. L. C. 2008, J. Geophys. Res. Space Phys., 113, A05221
- Echer, E., Tsurutani, B. T., & Gonzalez, W. D. 2013, J. Geophys. Res. Space Phys., 118, 385
- Gieseler, J., Dresing, N., Palmroos, C., et al. 2023, Front. Astron. Space Sci., 9,
- Gopalswamy, N., Lara, A., Yashiro, S., & Howard, R. A. 2003, ApJ, 598, L63 Gopalswamy, N., Nunes, S., Yashiro, S., & Howard, R. A. 2004, Adv. Space Res., 34, 391
- Gopalswamy, N., Yashiro, S., Stenborg, G., et al. 2009, Earth Moon Planets, 104,
- Gosling, J. T., & McComas, D. J. 1987, Geophys. Res. Lett., 14, 355
- Gosling, J. T., McComas, D. J., Phillips, J. L., & Bame, S. J. 1991, J. Geophys. Res. Space Phys., 96, 7831
- Greenwald, R. A., Bristow, W. A., Sofko, G. J., et al. 1995, J. Geophys. Res. Space Phys., 100, 19661
- Heinemann, S. G., Temmer, M., Farrugia, C. J., et al. 2019, Sol. Phys., 294, 121 Howard, R. A., Moses, J. D., Vourlidas, A., et al. 2008, Space Sci. Rev., 136, 67 Isavnin, A. 2016, ApJ, 833, 267
- Kaiser, M. L., Kucera, T. A., Davila, J. M., et al. 2008, Space Sci. Rev., 136, 5 Kataoka, R., Ebisuzaki, T., Kusano, K., et al. 2009, J. Geophys. Res. Space Phys., 114, A10102
- Kay, C., Nieves-Chinchilla, T., Hofmeister, S. J., & Palmerio, E. Space 2022, Weather, 20, e2022SW003165
- Kilpua, E. K. J., Liewer, P. C., Farrugia, C., et al. 2009, Sol. Phys., 254, 325
- Kilpua, E. K. J., Isavnin, A., Vourlidas, A., Koskinen, H. E. J., & Rodriguez, L. 2013, Ann. Geophys., 31, 1251
- Kilpua, E. K. J., Balogh, A., von Steiger, R., & Liu, Y. D. 2017a, Space Sci. Rev., 212, 1572
- Kilpua, E. K. J., Koskinen, H. E. J., & Pulkkinen, T. I. 2017b, Liv. Rev. Sol. Phys., 14, 1614
- Kilpua, E. K. J., Good, S. W., Palmerio, E., et al. 2019, Front. Astron. Space Sci.,
- Klein, L. W., & Burlaga, L. F. 1982, J. Geophys. Res.: Space Phys., 87, 613 Lapenta, G., Pucci, F., Goldman, M. V., & Newman, D. L. 2020, ApJ, 888, 104 Lemen, J. R., Title, A. M., Akin, D. J., et al. 2012, Sol. Phys., 275, 17 Li, L. P., Zhang, J., Li, T., Yang, S. H., & Zhang, Y. Z. 2012, A&A, 539, A7 Linan, L., Pariat, É., Moraitis, K., Valori, G., & Leake, J. 2018, ApJ, 865, 52 Linan, L., Pariat, É., Aulanier, G., Moraitis, K., & Valori, G. 2020, A&A, 636,
- A41 Liu, Y., Shen, F., & Yang, Y. 2019, ApJ, 887, 150 Lugaz, N., Salman, T. M., Winslow, R. M., et al. 2020, ApJ, 899, 119
- Maharana, A., Isavnin, A., Scolini, C., et al. 2022, Adv. Space Res., 70, 1641 Maharana, A., Scolini, C., Schmieder, B., & Poedts, S. 2023, A&A, 675, A136
- Masías-Meza, J. J., Dasso, S., Démoulin, P., Rodriguez, L., & Janvier, M. 2016, A&A, 592, A118
- Mays, M. L., Taktakishvili, A., Pulkkinen, A., et al. 2015, Sol. Phys., 290, 1775 McComas, D. J., Bame, S. J., Barker, P., et al. 1998, Space Sci. Rev., 86, 563

- Menvielle, M., Lathuillère, C., Bruinsma, S., & Viereck, R. 2007, Ann. Geophys., 25, 1949
- Menvielle, M., Iyemori, T., Marchaudon, A., & Nosé, M. 2010, Geomagnetic Observations and Models (Springer), 183
- Palmerio, E., Scolini, C., Barnes, D., et al. 2019, ApJ, 878, 37
- Palmerio, E., Lee, C. O., Richardson, I. G., et al. 2022, Space Weather, 20, e2022SW003215
- Pesnell, W. D., Thompson, B. J., & Chamberlin, P. C. 2012, Sol. Phys., 275, 3 Poedts, Stefaan, Lani, Andrea, Scolini, Camilla, et al. 2020, J. Space Weather Space Clim., 10, 57
- Pomoell, Jens, & Poedts, S. 2018, J. Space Weather Space Clim., 8, A35 Richardson, I. G., & Cane, H. V. 2010, Sol. Phys., 264, 1573
- Rodriguez, L., Zhukov, A. N., Dasso, S., et al. 2008, Ann. Geophys., 26, 213
- Rodriguez, L., Zhukov, A. N., Cid, C., et al. 2009, Space Weather, 7, S06003 Rouillard, A. 2011, J. Atmosph. Sol.-Terr. Phys., 73, 1201
- Salman, T. M., Winslow, R. M., & Lugaz, N. 2020, J. Geophys. Res. Space Phys., 125, e2019JA027084
- Scherrer, P. H., Schou, J., Bush, R. I., et al. 2012, Sol. Phys., 275, 207
- Schmieder, B., Démoulin, P., & Aulanier, G. 2013, Adv. Space Res., 51, 1967 Schmieder, B., Kim, R. S., Grison, B., et al. 2020, J. Geophys. Res. Space Phys.,
- Scolini, C., Verbeke, C., Poedts, S., et al. 2018, Space Weather, 16, 754
- Scolini, C., Rodriguez, L., Mierla, M., Pomoell, J., & Poedts, S. 2019, A&A, 626, A122
- Scolini, C., Chané, E., Temmer, M., et al. 2020, ApJS, 247, 21
- Shiota, D., & Kataoka, R. 2016, Space Weather, 14, 56
- Smith, C. W., L'Heureux, J., Ness, N. F., et al. 1998, Space Sci. Rev., 86, 613
- Song, H. Q., Zhang, J., Cheng, X., et al. 2020, ApJ, 901, L21
- Sow Mondal, S., Sarkar, A., Vaidya, B., & Mignone, A. 2021, ApJ, 923, 80 St. Cyr, O., Plunkett, S., Michels, D., et al. 2000, J. Geophys. Res., 105, 18169
- Stone, E. C., Frandsen, A., Mewaldt, R., et al. 1998, Space Sci. Rev., 86, 1 Taktakishvili, A., MacNeice, P., & Odstrcil, D. 2010, Space Weather, 8, S06007
- Temmer, M., Reiss, M. A., Nikolic, L., Hofmeister, S. J., & Veronig, A. M. 2017, ApJ, 835, 141
- Thernisien, A. 2011, ApJS, 194, 33
- Török, T., Downs, C., Linker, J. A., et al. 2018, ApJ, 856, 75 Van der Harten, R. J., & Clark, K. 1995, Space Sci. Rev., 71, 23
- Verbeke, C., Pomoell, J., & Poedts, S. 2019, A&A, 627, A111
- Verbeke, C., Schmieder, B., Démoulin, P., et al. 2022, Adv. Space Res., 70, 1663
- Webb, D. F., & Howard, T. A. 2012, Liv. Rev. Sol. Phys., 9, 1614
- Winslow, R. M., Lugaz, N., Schwadron, N. A., et al. 2016, J. Geophys. Res. Space Phys., 121, 6092
- Winslow, R. M., Scolini, C., Lugaz, N., & Galvin, A. B. 2021, ApJ, 916, 40 Xie, H., Ofman, L., & Lawrence, G. 2004, J. Geophys. Res. Space Phys., 109, A03109
- Yashiro, S., Gopalswamy, N., Michalek, G., et al. 2004, J. Geophys. Res. Space Phys., 109, A07105
- Yashiro, S., Michalek, G., & Gopalswamy, N. 2008, Ann. Geophys., 26, 3103 Zhang, J., Richardson, I. G., Webb, D. F., et al. 2007, J. Geophys. Res. Space Phys., 112, A10102
- Zhang, J., Temmer, M., Gopalswamy, N., et al. 2021, Prog. Earth Planet. Sci., 8,
- Zuccarello, F. P., Pariat, E., Valori, G., & Linan, L. 2018, ApJ, 863, 41